

Open Access: ISSN 1847-9286 www.jESE-online.org

Original scientific paper

Electrochemical detection of melatonin using Gd-doped ZnO nanoparticles modified carbon paste electrode

Mamata Prabhugaonkar¹, Jyothi H. Kini², Bahaddurghatta Eshwaraswamy Kumara Swamy³,⊠ and Lamabani Shivlanaik Manjunatha³

¹Post-Graduate Department of Chemistry, St. Xavier's College, Mapusa-Goa, India

²Department of P.G. studies in Industrial Chemistry, Government Arts and Science College (Autonomous), Karwar, Uttara Kannada, Karnataka, India

³Department of P.G. Studies and Research in Industrial Chemistry, Kuvempu University, Jnana Sahyadri, Shankaraghatta 577451, Shimoga, Karnataka, India

Corresponding authors: [™]<u>kumaraswamy21@yahoo.com</u>

Received: July 29, 2025; Accepted: October 9, 2025; Published: October 23, 2025

Abstract

In this work, we report the synthesis of gadolinium-doped ZnO nanoparticles (GZ Nps) with varying dopant concentrations (2, 5 and 10 % GZ Nps) to detect melatonin (MEL) through the fabrication of the modified carbon paste electrode (MCPE). Additionally, these Nps are examined for biomedical research and as a photocatalyst for the degradation of Rhodamine B dye. The study is focused on synthesizing GZ Nps using a sustainable green approach incorporating phytochemicals sourced from Tabernaemontana divaricata (T. divaricata) in the simple, economical and environmentally friendly co-precipitation method. Further, the analysis of as-synthesized GZ Nps by X-ray powder diffraction, field emission scanning electron microscopy and transmission electron microscopy analysis confirmed spherical morphology and better crystallinity with lesser agglomeration when the dopant ion concentration was increased. GZ Nps served as an effective photocatalyst for the degradation of Rhodamine B dye, achieving maximum degradation efficiency of 96.70 % for 2 % GZ sample. Furthermore, the antibacterial activity was tested using inhibitory zone radius measurements. In electrochemical studies using cyclic voltammetry and differential pulse voltammetry techniques, it was found that 5%GZ Nps, utilized to fabricate a GZ Nps modified carbon paste electrode (GZ/MCPE), showed excellent sensitivity for MEL alone and for the simultaneous detection of ciprofloxacin and MEL. By changing MEL concentrations, the limit of detection of MEL was determined to be 7.95 μ M.

Keywords

Semiconducting nanomaterial; rare-earth doping; *Tabernaemontana divaricata*; antibacterial activity; photocatalyst; electrochemical sensor; drugs

Introduction

The world as we know it faces numerous serious environmental problems that impact human health, aquatic life, and water resources, primarily due to water contamination. The primary source of water pollution is industrial effluents, which contain carcinogenic compounds, synthetic dyes, and pigments. These result from the substantial volume of untreated organic waste discharged into the environment. The textile industry is a significant consumer of synthetic dyes, representing around 60 % of total dye consumption. In the field of vivid colour exploration, a wide range of frequently reported artificial dyes are encountered, such as methyl orange, methyl violet, methylene blue, malachite green, and rhodamine B, which have an impact on many aspects of human life [1,2]. Synthetic dye molecules exhibit exceptional stability, rendering them resistant to various environmental factors. One example is rhodamine B (RB), a dye with a complicated structure that is challenging to break down and has high toxicity. RB dye is frequently used as a colouring agent, photosensitizer, water tracer, and fluorescent marker for microscopic structural investigation, in biomedical research, and in a variety of other industries. Moreover, human exposure to RB dye can result in ocular damage, irritation, and extreme mouth noxiousness [3-5].

Several processes have been used to study metal oxide applications, including flocculation, reverse osmosis, chemical oxidation, activated carbon adsorption, and biological therapies [6]. The n-type ZnO semiconductor serves as a promising catalyst for various applications, including gas sensors, photocatalysts, photoanodes, and light-emitting diodes. ZnO has a high binding energy of ~60 meV, a hexagonal wurtzite structure, and an ionic radius of 7.4 nm. It has merits due to nontoxicity, durability, and good biocompatibility compared to conventional organic materials [7]. Nevertheless, its 3.37 eV direct bandgap, which absorbs only 4 % of solar spectrum light, and rapid photoexcited charge carrier recombination restrict the photocatalytic effectiveness of ZnO. Several methods have been used to boost the catalytic activity and increase the light absorption capacity to overcome these limitations [8,9]. Nowadays, lanthanides are universal in every technology owing to their unique properties and multitude of applications. Doping Gd³⁺ enhances its photocatalytic performance by reducing the band gap and utilizing visible sunlight because this method provides good light absorption efficiency and an increase in the rate of charge transfer (e⁻ - h⁺ pairs), both of which contribute to an enhancement in photocatalytic activity [10,11]. Gadolinium as a dopant is considered a good choice for doping into a metal oxide matrix as it tends to increase charge separation, enhance the surface area, and reduce the size of nanoparticles (Nps). In addition, the half-filled 4f⁷ orbital of Gd³⁺ can easily trap the photogenerated electron from the metal oxide surface, making it useful in photocatalytic applications [12,13].

Green synthesis offers numerous advantages compared to conventional synthesis methods, including reduced reliance on toxic chemicals, lower energy consumption, diminished production of hazardous byproducts, and the promotion of sustainability through the use of renewable resources such as plant extracts, microorganisms, DNA, and proteins [14,15]. This study pioneers the biomediated synthesis of gadolinium-doped ZnO nanoparticles (GZ Nps) using *Tabernaemontana divaricata* (*T. divaricata*) leaf extract. *T. divaricata* is a versatile plant with medicinal and cosmetic properties and is called by different names, such as crape jasmine, pinwheel flower, Chandani, or Anant. The aqueous leaf extract of this plant is very rich in bioactives that play a crucial role in stabilizing/capping agents. The bio-actives present in this leaf extract are proteins, flavonoids, phenols, saponins, tannins, alkaloids, diterpenes, carbohydrates, and phytosterols. According to the literature reviewed, the synthesis of GZ Nps (2 % GZ, 5 % GZ and 10 % GZ Nps) using *T. divaricata* leaf extract is being reported for the first time [16,17].

A growing global public health concern is the emergence of harmful microorganisms resistant to many drugs. Traditional methods of fighting these resistant strains involve the use of antibiotics, which have drawbacks and can negatively affect non-target organisms. This may encourage the further development of resistance. The small size and high surface area-to-volume ratio make Nps a potential target for antibacterial studies. ZnO Nps have shown bactericidal properties against a variety of microorganisms. ZnO Nps can enter bacterial cells through the cell wall, accumulate within the cell, and induce apoptosis due to their nanoscale range [18]. It has also been reported that ZnO has bactericidal properties by generating reactive oxygen species. This work examines the potential synergies between Gd and ZnO nanoparticles in limiting microbial growth through the use of sustainable manufacturing processes and the incorporation of dopant components. In addition to this, the doped ZnO Nps have surprisingly proven an interesting application in various healthcare products. Hence, we test the antibacterial activity of the as-synthesized samples against Gram-positive bacteria (Staphylococcus aureus, Bacillus subtilis) and Gram-negative bacteria (Escherichia coli, Pseudomonas aeruginosa) by employing the agar well diffusion method [19,20]. In addition to improving our understanding of how GZ Nps interact with biological systems, this all-encompassing approach has the potential to lead to the development of potent antimicrobial therapies. Numerous investigations have been conducted on antibacterial properties of ZnO Nps and doped ZnO Nps [21-23].

Melatonin (MEL) is a hormone related to several diseases and also plays an important role in the sleep cycle. Its quantities vary during the day with the cardiac cycles. Therefore, medical professionals need to detect MEL levels in the body to know its signalling pathway and its effect on the endocrine system [24,25]. Ciprofloxacin hydrochloride (CP) is a second-generation fluoroquinolone antibiotic chemically defined as 1-cyclopropyl-6-fluoro-1, 4-dihydro-4-oxo-7-(1-piperazinyl)-3-quinoline carbo-xylic acid, monohydrochloride. CP is extensively utilized for the treatment of infectious disorders in cattle, poultry, and people, encompassing respiratory, urinary tract, gastrointestinal, ocular, and dermatological infections. Excessive ingestion of CP may result in tendon rupture and chondrotoxic effects in juvenile animals, as well as photo-toxicity, allergies, diarrhea, nausea, liver function changes, headaches, and vomiting in humans. Extended exposure to CP can have several consequences, including immunotoxicity, carcinogenicity, hypertension, genotoxicity, and endocrine disruption. The presence of CP and other antibiotic residues in the environment raises significant concerns over the potential growth of antibiotic-resistant bacteria [26,27].

The advancement of rapid, sensitive, and efficient methodologies for monitoring antibiotic concentrations in diverse matrices, including food, medicines, and water samples, is a prominent research focus. Therefore, quantitative analysis of MEL and CP is essential for the medical treatment of many such diseases. Among several analytical techniques, the electrochemical method of analysis has been considered an adequate technique for the determination of MEL and CP due to its simplicity, cost-effectiveness, speedy response, and sensitivity. Voltammetric techniques play a significant role in detecting these drugs with the aid of sensors [28-31].

The doped ZnO samples possess excellent electrochemical activities and superior electron transfer properties, which could be employed in optoelectronics, biomedical, and environmental applications as electrochemical sensors, biosensors, gas sensors, and so on, as reported in the literature [32-36]. However, there is limited literature on MEL detection using bio-mediated synthesized doped ZnO as an electrode material. Our current research work describes GZ Nps modified carbon paste electrode (GZ/MCPE) for MEL determination using electrochemical techniques like cyclic voltammetry (CV) and differential pulse voltammetry (DPV). We present, for the first time, the application of GZ/MCPE as an

electrochemical sensing material for the detection of MEL and the simultaneous detection of MEL and CP. GZ/MCPE exhibited enhanced redox kinetics, stability, and sensitivity by employing CV and DPV.

Experimental

Materials and chemicals

The leaves of T. divaricata plants were gathered from Mandrem village, Goa, India. Zinc nitrate hexahydrate ($Zn(NO_3)_2 \cdot 6H_2O$) and gadolinium(III) nitrate hexahydrate ($Gd(NO_3)_3 \cdot 6H_2O$), sodium hydroxide (NaOH), rhodamine B ($C_{28}H_{31}ClN_2O_3$), melatonin, ciprofloxacin were of analytic grade ordered from Merck Life Science Private Limited, Mumbai, India, monosodium and disodium orthophosphate based phosphate buffer (PB) solutions from HiMedia company, Mumbai, India and were utilized in the procedure without any additional purification.

Preparation of leaf extract

50 g of fresh leaves of *T. divaricata* were taken and washed with distilled water to remove surface impurities. The leaves were cut into small pieces and heated at 60 °C for two hours in a beaker filled with 200 mL of distilled water. Subsequently, the extract was allowed to cool to attain room temperature and filtered through Whatman filter paper no. 41. The filtrate obtained was refrigerated and used as the aqueous leaf extract for the bio-mediated synthesis of ZnO Nps and GZ Nps.

Synthesis of ZnO and gadolinium-doped ZnO nanoparticles

The $Zn_{1-x}Gd_xO$ (x = 0, 0.02, 0.05, 0.1), abbreviated as undoped ZnO, 2% GZ, 5% GZ and 10% GZ Nps, respectively, were synthesized by the co-precipitation method. 2.0 g of zinc nitrate hexahydrate was dissolved in 50 mL of distilled water and heated at 60 °C with continuous simultaneous stirring at room temperature for 30 minutes, followed by dropwise addition of *T. divaricata* leaf extract. Then, 2 M NaOH was incrementally introduced until the solution reached a stable pH of 12. The solution was further stirred for 2 hours. The obtained white precipitate was filtered using a vacuum filtration technique and Whatman filter paper no. 41. The precipitate was air-dried at room temperature and then calcined at 400 °C in a muffle furnace. For GZ Nps samples, a similar procedure was followed, and an appropriate amount of gadolinium (III) nitrate hexahydrate was used as a dopant to synthesise $Zn_{1-x}Gd_xO$ (x = 0, 0.02, 0.05, 0.1) to get GZ Nps, which were then labelled as 2% GZ, 5% GZ and 10% GZ Nps, respectively [37].

Characterization of ZnO and gadolinium-doped ZnO nanoparticles

The synthesized undoped ZnO and GZ Nps were characterized using various techniques. The X-ray powder diffraction (XRD) pattern for assessing the crystalline characteristics of the samples was obtained utilizing a Rigaku Mini Flex benchtop X-ray diffractometer, employing Cu K α radiation (λ = 0.1546 nm) across a 2 θ range of 20 to 80° for phase identification, with an acceleration voltage of 40 kV and a current of 40 mA. An ultra-silicon strip detector was employed to detect the reflected X-ray beam. To identify possible functional groups in the samples, Fourier transform infrared spectroscopy (FTIR) spectra were recorded in the range of 4000 to 400 cm⁻¹ using a Thermo-scientific Nicolet iS5 FTIR spectrophotometer, involving the KBr press pellet formation technique. The optical band gap of the synthesized samples was found by plotting the Tauc's plot using the ultraviolet-visible spectroscopy (UV-Vis) data recorded in the range 200 to 800 nm using a Shimadzu UV-1800 spectrophotometer. The average particle size and surface morphology were analysed using transmission electron microscopy (TEM), JEOL JEM-2100 Plus Electron Microscope, and field emission scanning electron microscopy (FESEM) model Quanta FEG 250 operating at 200 and 20 kV, respectively.

Photocatalytic studies

The photocatalytic behaviour of undoped and GZ Nps was studied using a mercury lamp reactor of power 239 watts. The distance between the mercury lamp and the reactor was \sim 8 cm. 0.05 g of catalyst was added to 50 mL of 10 ppm RB dye solution and kept in the dark to attain adsorption-desorption equilibrium for 30 minutes. The pH of the reaction mixture was maintained at 8. The solution was then exposed to light inside the reactor. At 15-minute intervals, the solution was placed in a quartz cuvette with a 1 cm path length to measure the absorbance using a UV-Vis spectro-photometer. To understand the effect of RB degradation, the degradation efficiency (D / %) was calculated for all the samples using Equation (1):

$$D = \frac{C_0 - C}{C_0} 100 \tag{1}$$

where C_0 and C are the initial and final concentrations of the RB dye at time t, respectively.

Antibacterial activity

The Gram-positive bacterial strains, such as *Bacillus subtilis* (MTCC-2395) and *Staphylococcus aureus* (MTCC-7443), and the Gram-negative bacterial strains, including *Escherichia coli* (MTCC-7410) and *Pseudomonas aeruginosa* (MTCC-1034), were used against which the samples were tested. The sterile saline solution was utilized to adjust the inoculum to approximately 5×10^5 CFU mL⁻¹. Samples were loaded into distinct wells with concentration ranges of 100 to 300 μ g mL⁻¹. This was done after dissolution at 37 °C on Muller-Hinton agar medium, using dimethyl sulfoxide (DMSO) as a reference. The diameter of the inhibitory zone was measured in nm.

Electrochemical investigation of melatonin at gadolinium-doped ZnO/modified carbon paste electrode

Instrumentation

The voltammetric study was conducted using a CHI-660C model (CH instrument, USA) with a conventional three-electrode system. The counter electrode was a Pt wire, the reference electrode was a saturated calomel electrode (SCE), and the working electrode was a carbon paste electrode (CPE), *i.e.* bare CPE (BCPE) and Gd-doped ZnO Nps modified CPE (GZ/MCPE).

Preparation of electrodes

BCPE was prepared manually by mixing a 70:30 weight ratio of graphite powder and silica gel for about 30 minutes. The GZ/MCPE was fabricated by adding 4 mg of GZ Nps to the above-indicated mixture in an agate mortar, following the same procedure as for the preparation of BCPE. Finally, the GZ/MCPE was selected to study other parameters throughout the experiment.

Results and discussion

XRD analysis

The X-ray powder diffraction (XRD) pattern of GZ Nps was recorded over the 20 to 80° range, as displayed in Figure 1. The Debye-Scherrer equation is used to estimate the average crystallite size (*L*) for all the synthesized samples. The crystallite size calculated for undoped and GZ Nps corresponding to the largest intensity plane is summarised in Table 1. The sharp and intense diffraction peaks are seen around the same angle positions. The observed diffraction peaks of 2% GZ indexed to (100), (002), (101), (102), (110), (103), (112) planes attributed to diffraction angles 31.854, 34.520, 36.328, 47.651, 56.683, 62.972 and 68.284° respectively agree well with hexagonal wurtzite structure of ZnO (JCPDS Card no 36-1451). Only ZnO peaks were observed in the diffraction patterns of all samples,

with no Gd peaks detected, demonstrating good purity of the produced materials [38]. Diffraction patterns indicate a significant reduction in peak intensity while transitioning from undoped to 10% GZ samples, resulting in diminished crystallinity of GZ Nps. With the reduction in peaks, it is also noticed that they have broadened and slightly shifted towards the lower 2θ angles, as seen in Figure 2, due to changes in lattice parameters [39]. Reported lattice parameters/constants a and c values in JCPDS data are a=0.324982 nm and c=0.520661 nm. The lattice constants a and c concerning the main peak (101) are calculated and tabulated in Table 1.

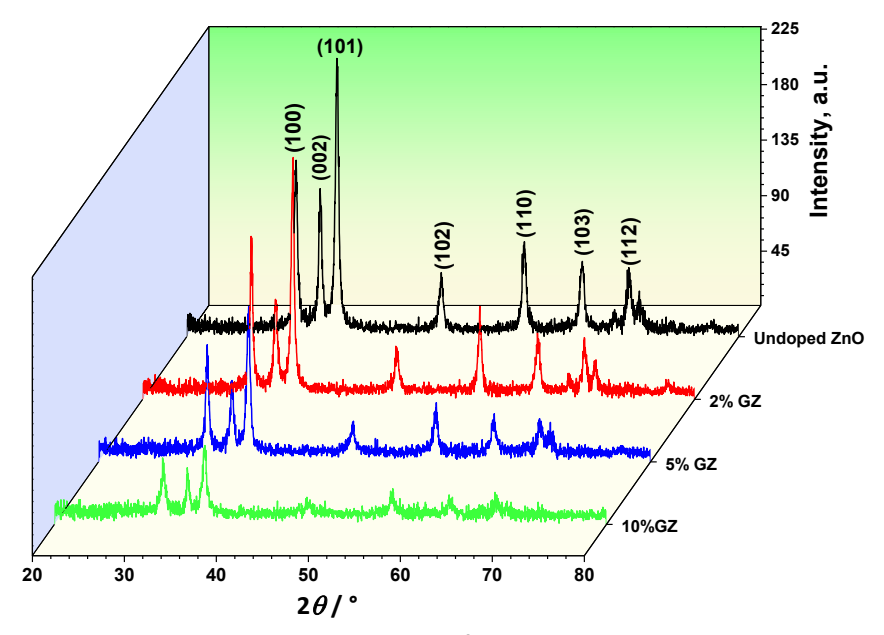


Figure 1. Stacked XRD patterns of undoped ZnO Nps and GZ Nps

Sample -	Scherrer method	Lattice parameters		
	<i>L</i> / nm	<i>a</i> / nm	<i>c</i> / nm	
Undoped ZnO	14.57	3.293	4.939	
2% GZ	16.95	3.295	4.942	
5% GZ	13.15	15 3.296		
10% GZ	11.72	3.297	4.944	

Table 1. Geometric parameters of ZnO Nps and GZ Nps

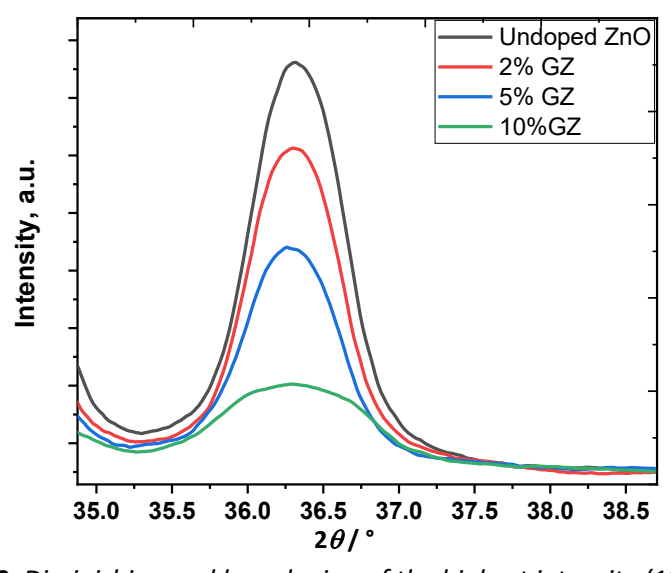


Figure 2. Diminishing and broadening of the highest intensity (101) plane

Fourier transform infrared spectroscopy studies

Fourier transform infrared spectroscopy (FTIR) studies of ZnO and GZ Nps provide insights into the functional group characteristics and chemical bonding within these materials. The leaf extract of *T. divaricata* was evaluated for the secondary bioactive compounds that facilitated the synthesis of ZnO and GZ Nps. Figure 3(a) shows the FTIR spectrum of T. divaricata leaf extract, illustrative of sharp absorption bands. The band at 672 cm⁻¹ might be due to flavone (a type of flavonoid). The bands at 1127, 1382, 1628 and 2929 cm⁻¹ correspond to C-O alcohol stretching, O-H phenolic bending medium, C=C alkene stretching of an aromatic ring, and C-H aldehydic stretching medium, respectively. Two commonly observed sharp bands around 2361 and 3434 cm⁻¹ are ascribed to the O=C=O group asymmetric stretching and O-H alcoholic stretching, respectively. The different functional groups and modes of vibration are due to the phytochemicals present in T. divaricata extract. The role of these phytochemicals is to reduce Zn²⁺ ions (bio-reduction) followed by chelation, which are then annealed to further degrade into ZnO Nps. The FTIR analysis across the studies indicates that doping ZnO with Gd alters the vibrational modes associated with the ZnO lattice. Figure 3(b) depicts the stacked FTIR spectra of undoped ZnO, 2% GZ, 5% GZ and 10% GZ Nps, wherein the metal oxide bond, such as the Zn-O bond, shows absorption bands at 453, 444, 453 and 450 cm⁻¹, respectively. Also, the Gd-O bond indicates its peaks around 852, 850 and 860 cm⁻¹ for 2% GZ, 5% GZ and 10% GZ Nps samples. Slight broad peaks in the range 1050 to 1082 cm⁻¹ are ascribed to the C-O bond stretch associated with primary alcohol. Carboxylate anion stretching vibration occurred at 1405, 1406 and 1403 cm⁻¹ for 2% GZ, 5% GZ and 10% GZ Nps, respectively. 1498 to 1609 cm⁻¹ is associated with amine (N-H) bending modes, and the weak peak at 2342 and 2924 cm⁻¹ is linked to atmospheric carbon dioxide and C-H stretching modes of alkyl chains. The broad bands around 3234 to 3431 cm⁻¹ correspond to O-H stretching vibrations of the adsorbed water molecules on the ZnO surface. Finally, the spectral changes, indicated by a slight shift towards a higher wavenumber with increased doping levels, suggest changes in bond lengths following the successful substitution of Zn²⁺ by Gd³⁺ ions.

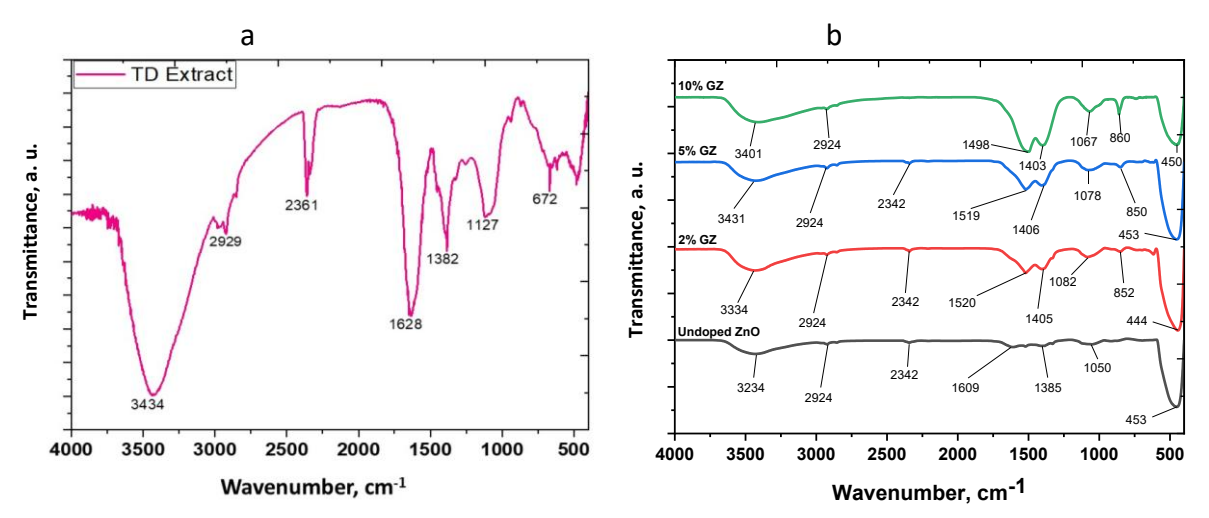


Figure 3. (a) FTIR spectra of T. divaricata leaf extract; (b) FTIR spectra of undoped ZnO Nps and GZ Nps

Ultraviolet-visible spectroscopy studies

Figure 4 shows the UV-Vis absorption spectra of as-synthesised undoped ZnO and GZ Nps, respectively. For undoped ZnO Nps, the peak centered at 370 nm is indicative of a high excitation binding energy that takes place at ambient temperature. Additionally, a single sharp absorption peak can be seen at approximately 369, 371 and 373 nm for the samples 2% GZ, 5% GZ and 10% GZ

Nps, respectively. As new sub-energy levels are added to the ZnO matrix with Gd addition, the shift of absorption peaks observed upon increasing Gd doping correlates to a red shift in absorption spectra. Additionally, the absorption peaks became somewhat broader from 2 to 10 % GZ Nps, which resulted in a decrease in crystallinity as the doping levels increased.

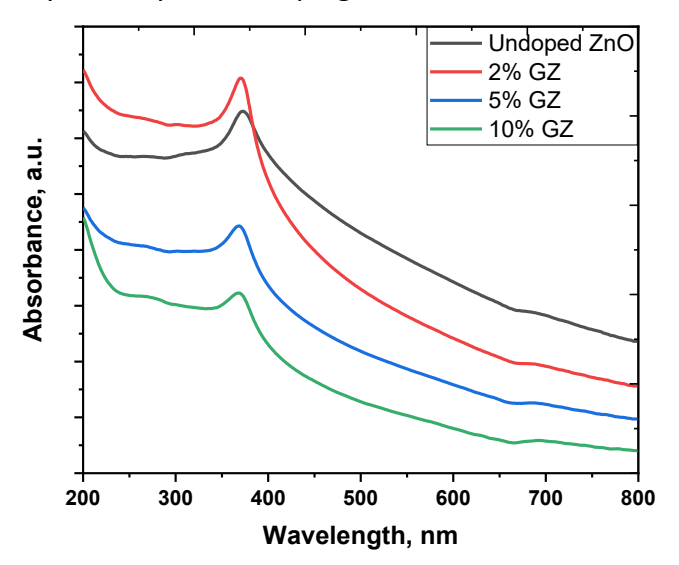


Figure 4. UV-Vis absorbance spectra of ZnO Nps and GZ Nps

The band gap value was calculated using Tauc's plot upon extrapolating the curves using Equation (2): $(\alpha h v)^2 = A (h v - E_g)$

where α is the absorption coefficient, h is Planck's constant, ν is the frequency, A is a constant and E_g is the optical bandgap energy of the materials. As seen in Figure 5, the Tauc's plots after extrapolating the straight lines down the x-axis yield the values of optical band gap energy (E_g).

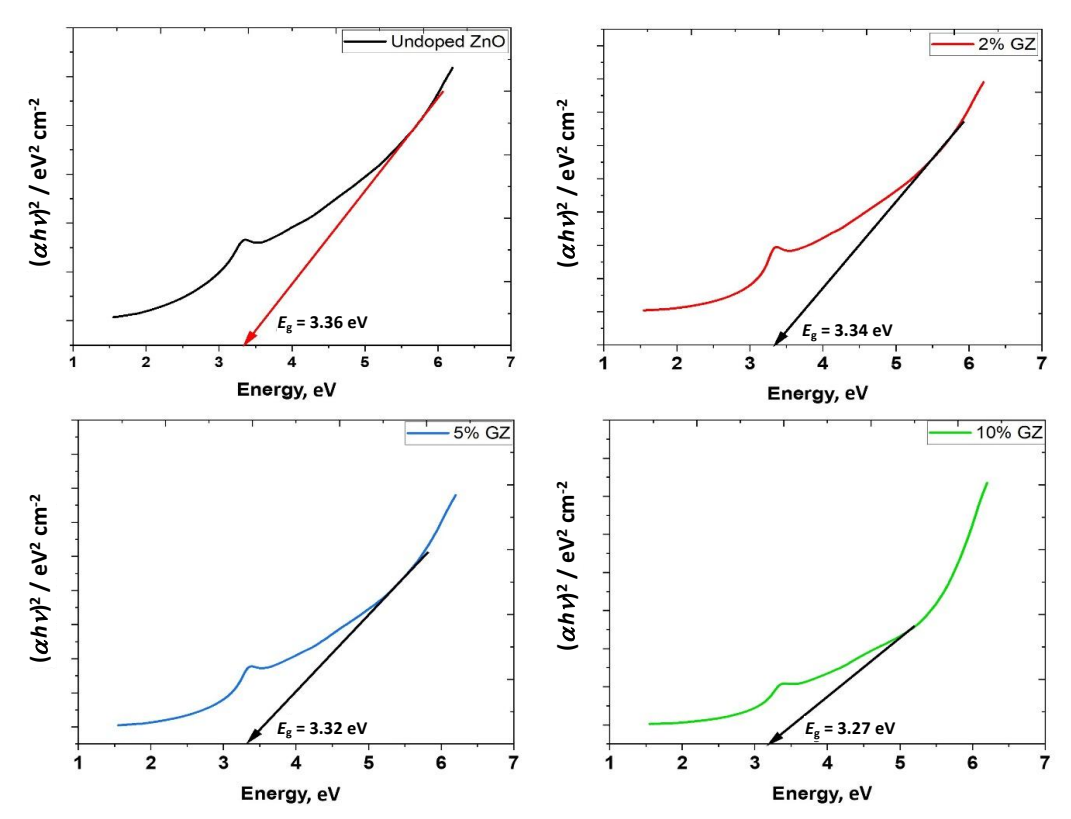


Figure 5. Tauc's plots of ZnO Nps and GZ Nps for optical band gap energy (E_g) determination

After extrapolation, the line's optical band gap values for undoped ZnO, 2% GZ, 5% GZ and 10% GZ Nps were 3.36, 3.34, 3.32 and 3.27 eV, respectively. The conclusions drawn from these band gap values are that the energy gap (E_g) values decrease as the Gd levels increase.

Field emission scanning electron microscopy analysis

Surface morphology was studied using FESEM for the biosynthesized samples. Figure 6 illustrates the FESEM images of pure ZnO and GZ Nps. It is evident from the images that all the samples are in nano-spherical shapes. However, it can be observed that there is a difference in the shape's curvature. The ZnO sample exhibits a rough spherical morphology; however, when the concentration of GZ nanoparticles increases from 2 to 10 %, these rough spheres are converted into smooth spherical forms [26]. The other change noted is the decrease in the agglomeration phenomenon (particle interaction through local forces) with increasing Gd concentrations.

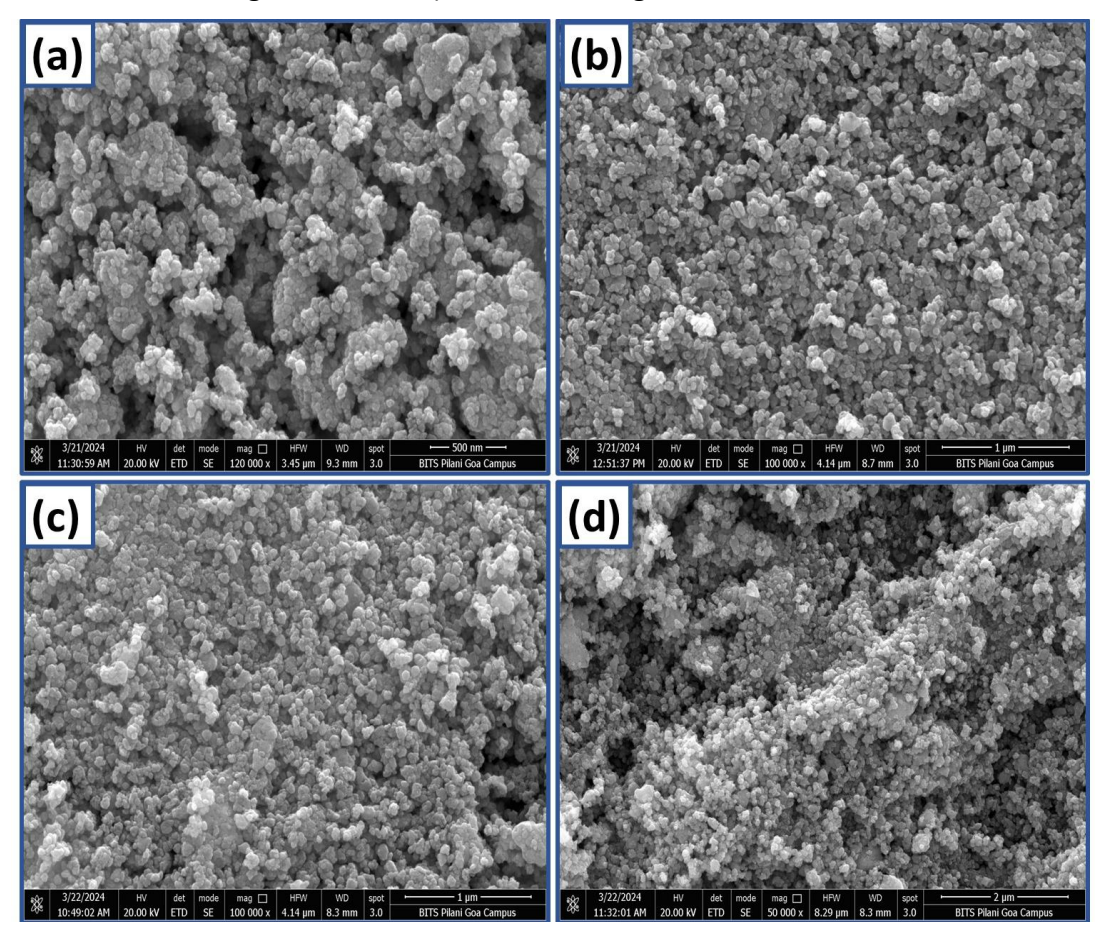


Figure 6. FESEM images of (a) undoped ZnO Nps, (b) 2% GZ Nps, (c) 5% GZ Nps and (d) 10% GZ Nps

The computed particle size (S) is presented in Table 2, detailing the dimensions of the Nps from FESEM and XRD data. The particle sizes derived from the FESEM study correspond with the XRD analysis.

Table 2. The crystallite size and particle size obtained from XRD data and FESEM images for the first three diffraction peaks

Sample	L ₍₁₀₀₎ / nm	L ₍₀₀₂₎ / nm	L ₍₁₀₁₎ / nm	S _{SEM} / nm
Undoped ZnO	16.106	16.276	16.841	20 - 50
2% GZ	20.020	14.399	17.801	20 - 40
5%GZ	16.862	13.287	15.541	20 - 40
10% GZ	11.005	13.539	12.782	10 - 40

Transmission electron microscopy analysis

TEM micrographs at various magnifications were used to analyse further the structure of the 5% GZ sample (Figure 7). The TEM pictures of 5% GZ exhibit a spherical-like morphology that closely aligns with the findings of FESEM, unequivocally demonstrating that ZnO crystal has successfully integrated the Gd³⁺ ions. Though the size and structure of Nps are not uniformly seen, very slight hexagon-shaped structures are visible in the images. The most intriguing finding is that the core particles of these structures are hexagonal-shaped ZnO, despite the smooth appearance of the outer surface observed due to a higher percentage of dopant ions. The selected area electron diffraction (SAED) pattern of 5% GZ displays concentric rings that belong to the hexagonal wurtzite structure of ZnO, which are consistent with XRD data. Also, the tiny shiny spots noticed on the rings belonging to (101) and (200) ZnO crystal planes arise from Bragg reflection from various crystallites that form a polynanocrystalline structure.

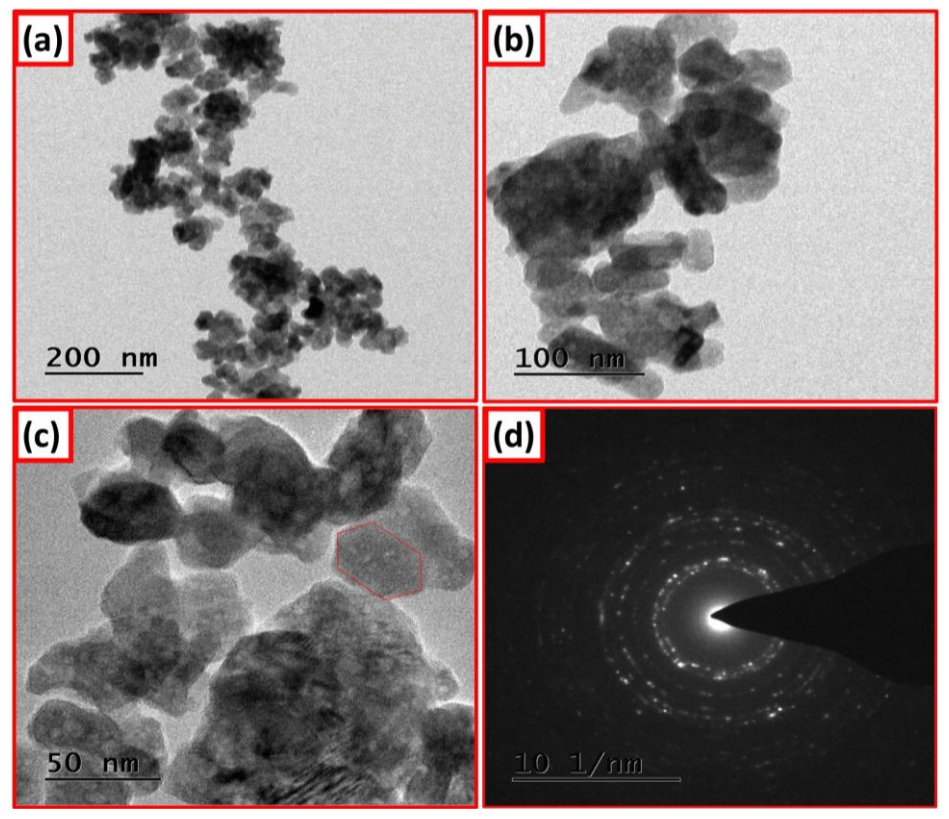


Figure 7. (a-c) TEM images of 5% GZ Nps at various magnifications, (d) SAED image of 5% GZ Nps

Photocatalytic analysis

RB dye degradation was used to measure the photocatalytic activity of ZnO Nps and GZ Nps under visible light irradiation. Figure 8a depicts the plot of the ratio of the final concentration of RB dye to its initial concentration (C/C_0) of RB dye versus irradiation time. The photolysis of RB dye in the presence of visible light with the catalyst at 0 min did not indicate any degradation efficiency, demonstrating the stability of the dye molecule. When a fixed amount of undoped ZnO is exposed for 120 min, only 86.72 % of the RB dye is degraded, while 2% GZ, 5% GZ and 10% GZ samples achieve 96.70, 89.21 and 84.33 % degradation efficiency, respectively, as shown in Figure 8c. Among these, 2% GZ exhibited the maximum degradation ability to break down the RB dye molecules. The comparison of the photocatalytic degradation efficiency of 2% GZ Nps catalyst with some other catalysts for RB dye degradation is presented in Table 3.

The degradation ability for 5% GZ and 10% GZ Nps got reduced upon an increase in Gd levels, which is assigned to the screening effect property, where a greater number of Gd³⁺ ions hinders the

light penetration depth into ZnO by traveling much farther than the space charge layer, making the recombination of electron-hole pairs quicker, decreasing the degradation ability.

Table 3. Comparison of photocatalytic degradation efficiency of 2% GZ Nps catalyst with some other catalysts for RB dye degradation

Catalyst	Synthesis method	Irradiation source	Time taken, min	D/%	Ref.
2% GZ	Co-precipitation	Hg lamp	120	96.70	This work
Co-ZnO/rGO	Electrospinning hydrothermal technique	Sunlight	420	95	[40]
Zn _{0.97} Ni _{0.03} O	Spray pyrolysis	Solar light	90	60.24	[41]
Au-ZnO	Centrifuge	UV light	180	95	[42]
Ni-doped ZnO	Simple solvothermal	Visible light	150	93	[43]

The degradation ability can be boosted by having the optimal Gd concentration compared to the undoped sample. The pseudo-first-order reaction kinetics is observed through degradation reactions, as confirmed by the slopes of the straight lines shown in Figure 8b.

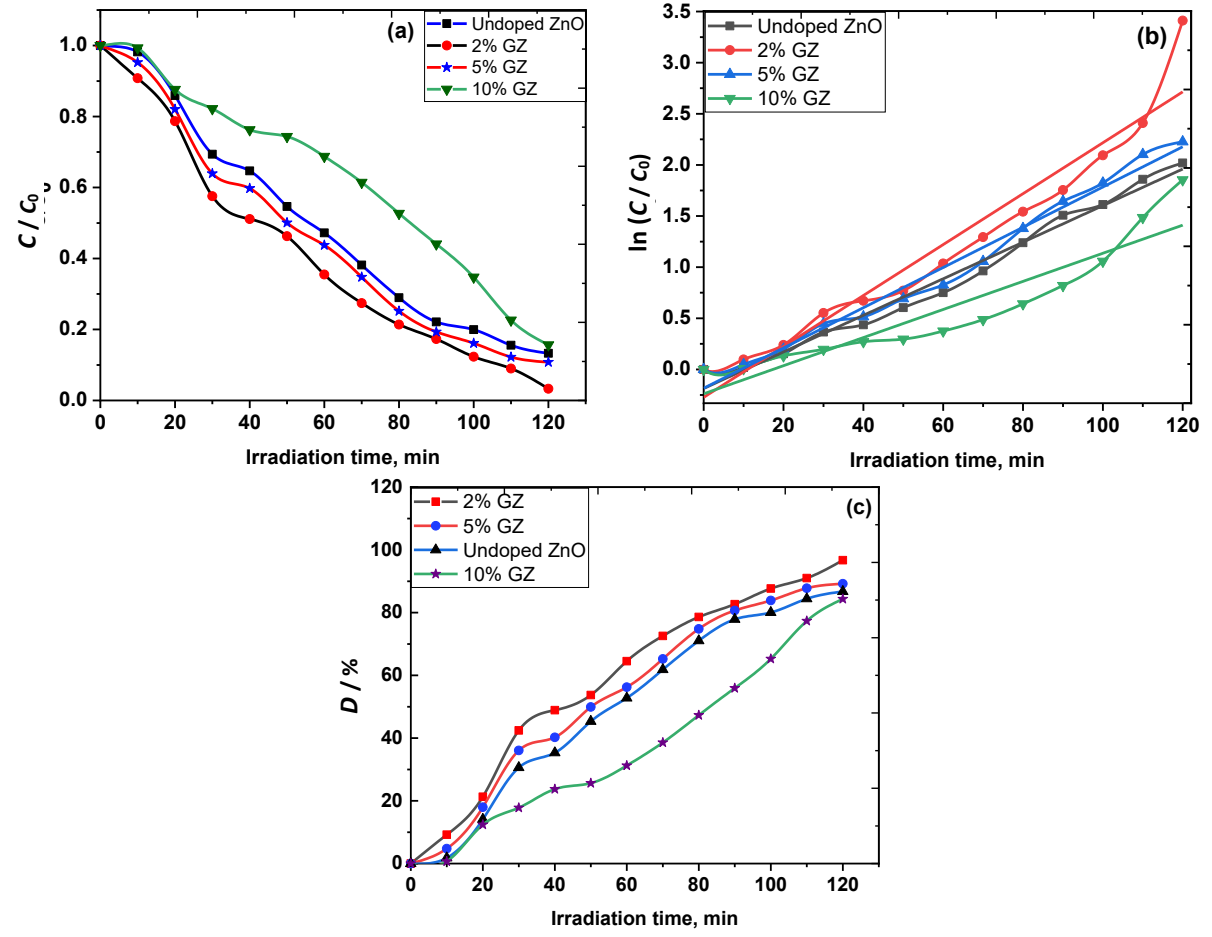


Figure 8. (a) Comparison of photocatalytic degradation activity of undoped ZnO and GZ Nps for RB dye vs. irradiation time, (b) reaction kinetic plot and (c) degradation efficiency of pure ZnO and GZ Nps

The slopes of the straight lines gave the apparent rate constants as 0.01789 min⁻¹ for undoped ZnO, 0.0249 min⁻¹ for 2% GZ, 0.01968 min⁻¹ for 5% GZ and 0.01379 min⁻¹ for 10% GZ samples. When ZnO Nps are photo-induced, having energy of a photon greater than the optical band gap energy of ZnO, electron and hole pairs are generated. If the separation between the electron (e⁻CB) and hole (h⁺VB) pairs is sustained, the photoexcited electron gets trapped in additional sub-energy levels created by Gd dopant where Gd³⁺ ion gets reduced to Gd²⁺ and trapped electron reacts with oxygen to yield superoxide anion radical which on further protonation generates hydroxyl (·OH) radical,

meanwhile, h^+_{VB} tends to react with water molecules to also similarly give hydroxyl radicals. The radicals generated in this process are commonly termed reactive oxygen species (ROS), which are the main agents responsible for degrading the dye molecule. The hydroxyl radicals generated from the interaction with e^-_{CB} and h^+_{VB} are the primary agents that interact with the dye molecule.

Antibacterial activity

The prepared GZ Nps were tested for their in vitro antibacterial activity against two Gram-positive and two Gram-negative bacterial strains via the agar well diffusion method. All of the substances had a zone of inhibition (ZOI) for various microorganisms at concentrations of 100, 200 and 300 μg mL⁻¹, taking dimethyl sulfoxide (DMSO) as a control. In our current work, DMSO itself had no inhibitory effect on the bacterial growth. For all the samples, at a concentration of 300 μg mL⁻¹, the utmost antibacterial effect was observed for all-inclusive bacterial strains (MTCC-7443, MTCC-2395, MTCC-7419, MTCC-1034). Only 2% GZ samples at 100 μg mL⁻¹ concentration had proven sensitivity towards *E. coli* bacteria, while the rest of the samples at the same concentration showed resistance. The undoped ZnO, 2% GZ and 10% GZ at 100µg mL⁻¹ concentration had proven inhibition sensitivity towards P. aeruginosa, E. coli, and B. subtilis, respectively. The 10% GZ Nps concentration of 200 μg mL⁻¹ could effectively obstruct the bloom of Gram-positive and Gram-negative bacterial strains, while undoped ZnO and 5% GZ Nps were both productive in combating two strains of bacteria (B. subtilis and E. coli). However, the undoped ZnO could target P. aeruginosa but did not show any efficacy towards S. aureus, as demonstrated by 5% GZ. To summarize, the increased inhibition of bacterial strains was best achieved with 10% GZ compared to undoped ZnO, possibly due to differences in ionic radii between Gd and Zn, as reported in the study [19]. Another major explanation for bacterial cell death is the production of ROS, such as superoxide anion radical, hydroxyl radical, and peroxide by metal oxides on the surface of the cells during exposure to light. Among these three ROS, the superoxide anion radical can damage DNA, lipids, and cellular proteins, potentially leading to cell death. Thus, the ZOI around the Nps is effectively depicted as a portrait of the antibacterial activity shown in Figure 9.

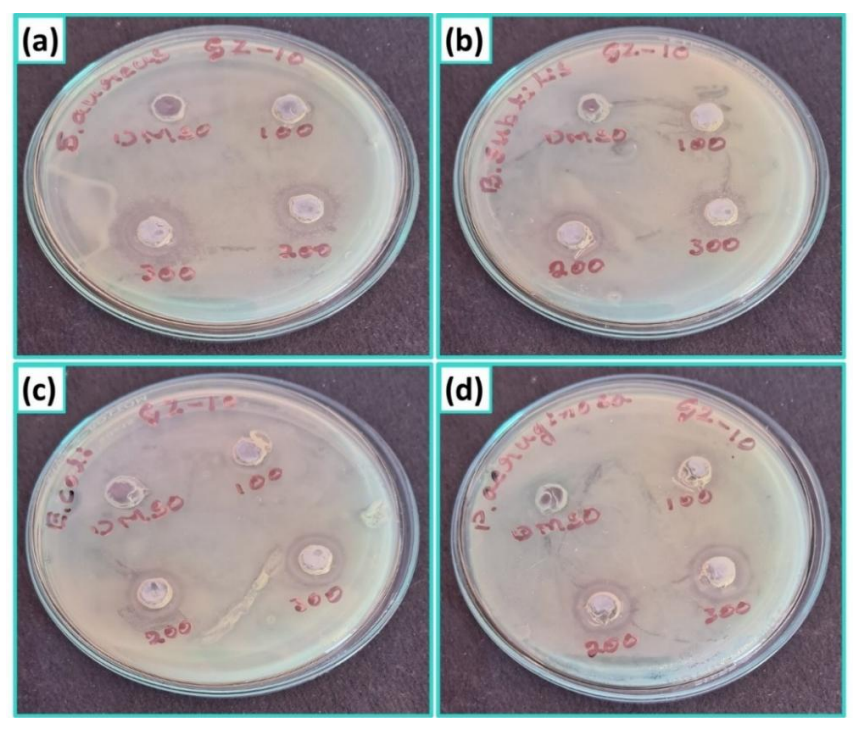


Figure 9. Agar plates of the 10% GZ Nps containing ZOI of Gram-positive (a) S. aureus, (b) B. subtilis and Gram-negative (c) E. coli and (d) P. aeruginosa bacterial strains

Standard K₄[Fe(CN)₆] reaction at BCPE and GZ/MCPE

The ROS generation is even more enhanced as Gd doping levels in ZnO matrix were increased due to Gd³⁺ ions substitution along Zn²⁺ sites, and this holds in the case of a 10% GZ sample.

Electrochemical investigation of melatonin at gadolinium-doped ZnO/modified carbon paste electrode

The comparison of electrochemical properties between BCPE and GZ/MCPE was carried out by employing the CV technique. The mass of synthesized GZ Nps (4 mg) was applied on the surface of CPE and investigated by CV with 1 mM $K_4[Fe(CN)_6]$ in 1 M KCl as a supporting electrolyte at a scan rate of 0.05 V s⁻¹. The results are displayed in Figure 10, which shows that the redox peak current at GZ/MCPE is significantly higher than at BCPE.

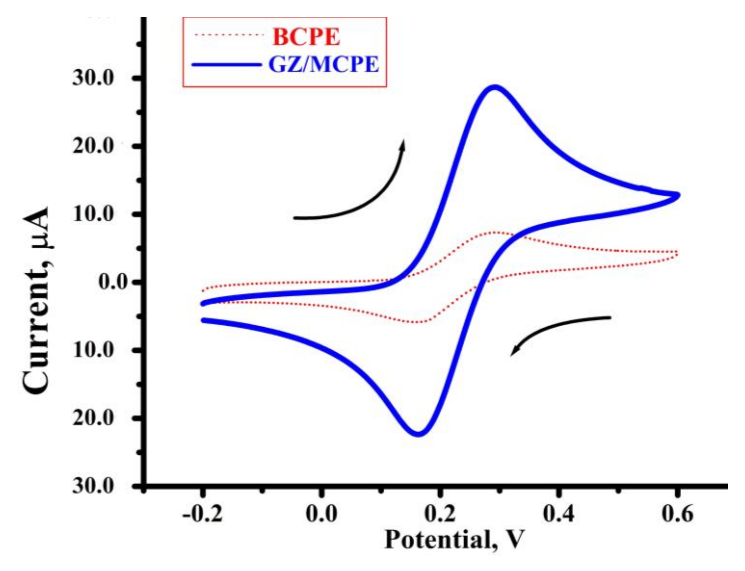


Figure 10. Cyclic voltammograms of 1 mM K_4 [Fe (CN) $_6$] · 3H $_2$ O in 1 M KCl of BCPE (red dotted line) and GZ/MCPE (blue line) at a sweep rate of 0.05 V s^{-1}

Electrochemical investigation of melatonin at BCPE and GZ/MCPE

The cyclic voltammograms of 10 μ M MEL in 0.2 M PB are displayed as a red dotted line for the BCPE, and a solid blue line for GZ/MCPE in Figure 11. A significantly enhanced oxidation peak current of MEL at GZ/MCPE, compared to BCPE, is observed at 0.63 and 0.60 V, respectively. Therefore, the fabricated GZ/MCPE showed better redox kinetics for MEL.

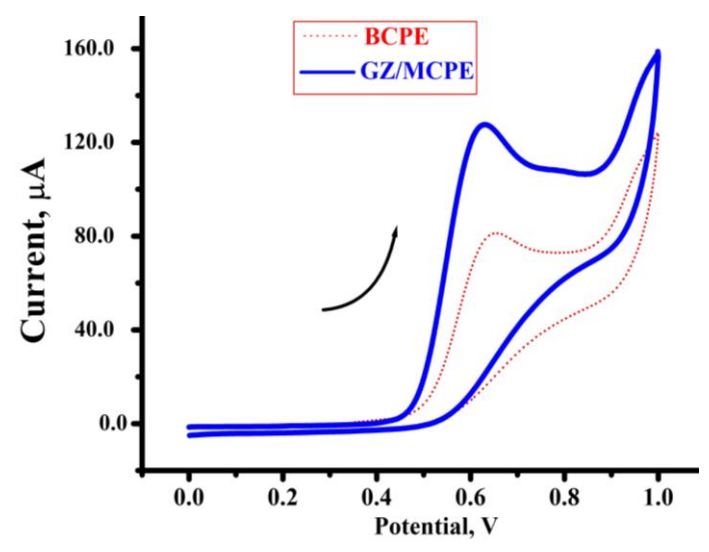


Figure 11. Cyclic voltammograms of 10 μ M MEL in 0.2 M PB (pH 7.4) at BCPE (red dotted line) and GZ/MCPE (blue solid line) at a sweep rate of 0.05 V s^{-1}

Concentration effect of melatonin at GZ/MCPE

To analyse the electrocatalytic activity, MEL was recorded by the DPV technique using GZ/MCPE in 0.2 M PB (pH 7.4), at 0.05 V s⁻¹. Figure 12(A) displays the DPV recordings for various concentrations of MEL from 20 to 80 μ M, which shows that the redox peak current was enhanced with an increase in the concentration of MEL at GZ/MCPE. A graph of peak current versus concentration is plotted in Figure 12(B), and the results strongly indicate that the redox peak current of MEL is directly dependent on the MEL concentration. The correlation coefficient was found to be R^2 = 0.9914, and the limit of detection (LOD) and limit of quantification (LOQ) were determined by Equations (3) and (4):

$$LOD = 3\sigma/P \tag{1}$$

$$LOQ = 10\sigma/P \tag{2}$$

where P is the slope value and σ is the value of standard deviation obtained from the linear graph. The LOD for MEL was established to be 7.95 μ M and the LOQ was 26.52 μ M.

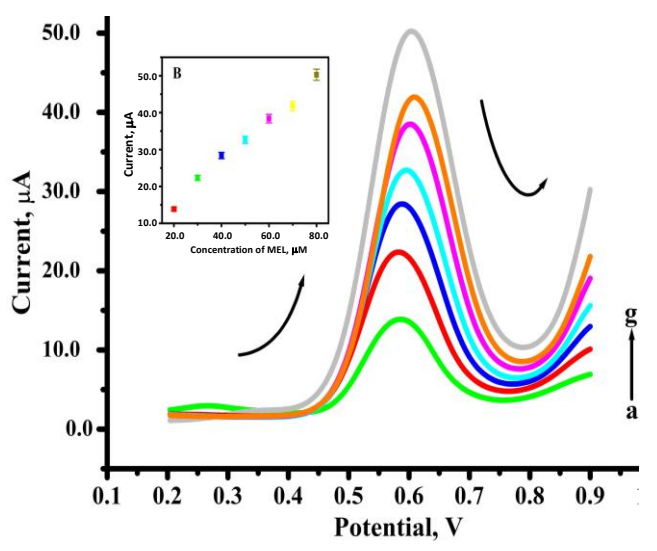


Figure 12. (A) DPV plots for the varying concentrations of MEL [a-20, b-30, c-40, d-50, e-60, f-70 and g- 80 μ M]at GZ/MCPE in 0.2M PB (pH 7.4), (B) plot of I_{pa} versus concentration of MEL

Simultaneous detection of MEL and ciprofloxacin

The proper detection of MEL and CP was examined at GZ/MCPE using the DPV technique. The redox peaks for MEL and CP were not clearly observed. Figure 13 shows that for BCPE, two low redox peak currents could be observed with anodic peak potential (E_{pa}) of 0.614 and 0.927 V, respectively.

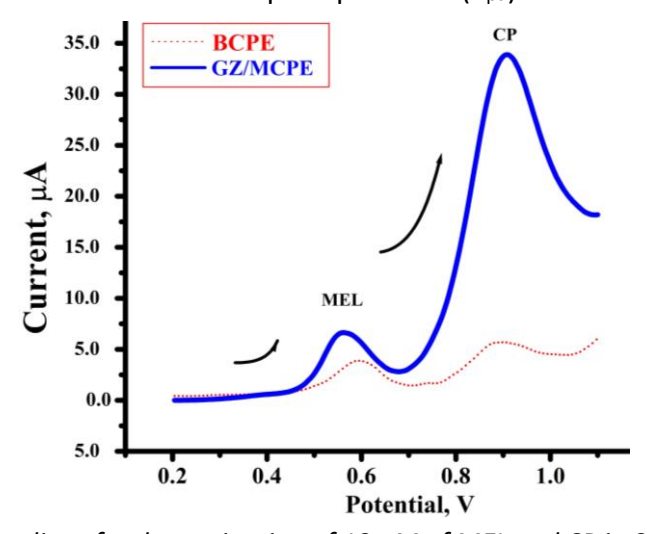


Figure 13. DPV recordings for determination of 10 μ M of MEL and CP in 0.2 M PB (pH 7.4) at BCPE (red dotted line) and GZ/MCPE (solid blue line)

At GZ/MCPE, however, two well-elucidated peaks are noticed with E_{pa} values detected at 0.583 and 0.897 V for MEL and CP, respectively. The potential difference between MEL and CP was revealed as 0.32 V, which confirms that GZ/MCPE shows excellent electrochemical behaviour in the simultaneous investigation of MEL and CP.

Conclusion

This study focuses on a plant-mediated route for synthesizing GZ Nps using T. divaricata leaf extract. The impact of doping on the optical and structural characteristics of ZnO was examined by utilizing characterization methods such as XRD, FTIR, UV-Vis, FE-SEM and TEM. 2% GZ Nps exhibited a significant degradation efficiency when the samples were exposed to RB degradation under Hg light irradiation for 120 minutes. Moreover, the degrading ability decreases as dopant levels rise. Compared to other samples, the 10% GZ Nps exhibited a substantial zone of inhibition and indicated effective antibacterial activity against all Gram-positive and Gram-negative bacterial strains. When compared to BCPE, synthesized GZ Nps have shown a remarkable sensitivity for MEL hormone by the voltammetric approach. By varying the MEL concentration from 20 to 80 μ M, the GZ/MCPE could attain a detection limit of 7.95 μ M for MEL and showed strong selectivity, which was supported by the simultaneous research of MEL and CP.

Funding: There is no funding

Conflict of interest: There is no conflict of interest

References

- [1] D. Dodoo-Arhin, T. Asiedu, B. Agyei-Tuffour, E. Nyankson, D. Obada, J. M. Mwabora, Photocatalytic degradation of Rhodamine dyes using zinc oxide nanoparticles, *Materials Today: Proceedings* **38** (2021) 809-815. https://doi.org/10.1016/j.matpr.2020.04.597
- [2] M. R. Ardani, A. L. Pang, U. Pal, M. A. S. M. Haniff, A. G. Ismail, A. A. Hamzah, W. A. Khanday, M. Ahmadipour, Ultrasonic-assisted synthesis of TiO₂-MWCNT nanocomposite with advanced photocatalytic efficiency for elimination of dye pollutions, *Diamond and Related Materials* **137** (2023) 110066. https://doi.org/10.1016/j.diamond.2023.110066
- [3] A. L. Pang, M. Saqlain Iqbal, N. Akmar Rejab, U. Pal, M. Aniq Shazni Mohammad Haniff, A. Ghadafi Ismail, A. Azlan Hamzah, M. Ahmadipour, Photocatalytic degradation of organic dye under UV light using CaCu₃Ti₄O₁₂ nanoparticles synthesized by sol-gel route: Effect of calcination temperature, *Inorganic Chemistry Communications* **150** (2023) 110462. https://doi.org/10.1016/j.inoche.2023.110462
- [4] T. L. Yusuf, B. O. Orimolade, D. Masekela, B, Mamba, N. Mabuba, The application of photoelectrocatalysis in the degradation of rhodamine B in aqueous solutions: a review, *RSC Advances* **12** (2022) 26176-26191. https://doi.org/10.1039/D2RA04236C
- [5] M. Lal, P. Sharma, L. Singh, C. Ram, Photocatalytic degradation of hazardous Rhodamine B dye using sol-gel mediated ultrasonic hydrothermal synthesized of ZnO nanoparticles, *Results in Engineering* **17** (2023) 100890. https://doi.org/10.1016/j.rineng.2023.100890
- [6] A. Piras, C. Olla, G. Reekmans, A.-S. Kelchtermans, D. de Sloovere, K. Elen, C. M. Carbonaro, L. Fusaro, P. Adriaensens, A. Hardy, C. Aprile, M. K. van Bael, Photocatalytic Performance of Undoped and Al-Doped ZnO Nanoparticles in the Degradation of Rhodamine B under UV-Visible Light: The Role of Defects and Morphology, *International Journal of Molecular Sciences* 23 (2022) 15459. https://doi.org/10.3390/ijms232415459
- [7] M. Toma, O. Selyshchev, Y. Havryliuk, A. Pop, D. R. T. Zahn, Optical and Structural Characteristics of Rare Earth-Doped ZnO Nanocrystals Prepared in Colloidal Solution, *Photochem* **2** (2022) 515-527. https://doi.org/10.3390/photochem2030036

- [8] S. Selvaraj, M. K. Mohan, M. Navaneethan, S. Ponnusamy, C. Muthamizhchelvan, Synthesis and photocatalytic activity of Gd doped ZnO nanoparticles for enhanced degradation of methylene blue under visible light, *Materials Science in Semiconductor Processing* **103** (2019) 104622. https://doi.org/10.1016/j.mssp.2019.104622
- [9] B. Palanivel, Md S. Hossain, R. R. Macadangdang Jr., S. S. Jude Dhas, A. M. Al-Enizi, M., Ubaidullah, W. K. Kim, S. Gedi, S. I. Arockiam, Effect of rGO support on Gd@ZnO for UV-visible-light-driven photocatalytic organic pollutant degradation, *Journal of Rare Earths* **41** (2023) 1525-1531. https://doi.org/10.1016/j.jre.2022.07.019
- [10] K. Safeen, A. Safeen, D. Arif, W. H. Shah, A. Ali, G. Ali, F. Hussain, N. Imran, A. Ullah Shah, A. Alataway, A.Z. Dewidar, H.O. Elansary, M. Al-Yafrsi, K.S. Ahmad, Tuning the Optical Properties of ZnO by Co and Gd Doping for Water Pollutant Elimination, *Water* 15 (2023) 1470. https://doi.org/10.3390/w15081470
- [11] Y.-X. Nguyen-Hong, T. V. H. Luu, V.-D. Doan, Green synthesis of Ce-doped ZnO nanoparticles using *Hedyotis capitellata* Leaf extract for efficient photocatalytic degradation of Methyl Orange, *Vietnam Journal of Chemistry* **59** (2021) 648-659. https://doi.org/10.1002/vjch.202100031
- [12] A. Mehtab, J. Ahmed, S. M. Alshehri, Y. Mao, T. Ahmad, Rare earth doped metal oxide nanoparticles for photocatalysis: A perspective, *Nanotechnology* **33** (2022) 142001. https://doi.org/10.1088/1361-6528/ac43e7
- [13] M. Zangeneh, H. A. Nedaei, H. Mozdarani, A. Mahmoudzadeh, M. Salimi, Enhanced cytotoxic and genotoxic effects of gadolinium-doped ZnO nanoparticles on irradiated lung cancer cells at megavoltage radiation energies, *Materials Science and Engineering: C* **103** (2019) 109739. https://doi.org/10.1016/j.msec.2019.109739
- [14] M._C. Naik, J. H. Kini, B. E. K. Swamy, S. Velho-Pereira, Sensor and antibacterial research of *Mussaenda frondosa* leaf extract assisted zinc oxide nanoparticles, *Sensing Technology* **2** (2024) 2385839. https://doi.org/10.1080/28361466.2024.2385839
- [15] M. Rafique, R. Tahir, S. S. A. Gillani, M. Bilal Tahir, M. Shakil, T. Iqbal, M. O. Abdellahi, Plant-mediated green synthesis of zinc oxide nanoparticles from *Syzygium Cumini* for seed germination and wastewater purification, *International Journal of Environmental Analytical Chemistry* **102** (2022) 23-38. https://doi.org/10.1080/03067319.2020.1715379
- [16] Md M. Rahman, M. A. Sayeed, K. P. Biplab, S. A. Siddique, Antidiabetic and cytotoxic activities of methanolic extract of *Tabernaemontana divaricata* (L.) leaves in alloxan induced mice, *Asian Journal of Pharmaceutical and Clinical Research* **5** (2012) 49-52.
- [17] A. Raja, S. Ashokkumar, R. Pavithra Marthandam, J. Jayachandiran, C. P. Khatiwada, K. Kaviyarasu, R. Ganapathi Raman, M. Swaminathan, Eco-friendly preparation of zinc oxide nanoparticles using *Tabernaemontana divaricata* and its photocatalytic and antimicrobial activity, *Journal of Photochemistry and Photobiology B: Biology* **181** (2018) 53-58. https://doi.org/10.1016/j.jphotobiol.2018.02.011
- [18] I. Ahmad, M. Y. Alshahrani, S. Wahab, A. I. Al-Harbi, N. Nisar, Y. Alraey, A. Alqahtani, M. A. Mir, S. Irfan, M. Saeed, Zinc oxide nanoparticle: An effective antibacterial agent against pathogenic bacterial isolates, *Journal of King Saud University-Science* **34** (2022) 102110. https://doi.org/10.1016/j.jksus.2022.102110
- [19] E. N. Danial, M. Hjiri, M. Sh. Abdel-wahab, N. H. Alonizan, L. El Mir, M. S. Aida, Antibacterial activity of In-doped ZnO nanoparticles, *Inorganic Chemistry Communications* **122** (2020) 108281. https://doi.org/10.1016/j.inoche.2020.108281
- [20] M. Devi, S. Sharma, P. Kumar, N. Thakur, G. Kumar, M. V. Sharma, A. J. Sharma, K. Kumar, A. Sharma, K. Jeet, N. Thakur, Antifungal, antibacterial and antioxidant activity of *Pinus roxburghii* mediated green synthesized zinc and gadolinium doped manganese oxide



- nanoparticles, *Colloids and Surfaces C: Environmental Aspects* **2** (2024) 100046. https://doi.org/10.1016/j.colsuc.2024.100046
- [21] S. Vinodhini, B. S. M. Vithiya, T. A. A. Prasad, Green synthesis of silver nanoparticles by employing the *Allium fistulosum, Tabernaemontana divaricata* and *Basella alba* leaf extracts for antimicrobial applications, *Journal of King Saud University Science* **34** (2022) 101939. https://doi.org/10.1016/j.jksus.2022.101939
- [22] C. Selvaraju, R. Karthick, R. Veerasubam, The Modification of Structural, Optical and Antibacterial Activity Properties of Rare Earth Gadolinium-Doped ZnO Nanoparticles Prepared by Co-Precipitation Method, *Journal of Inorganic and Organometallic Polymers and Materials* **29** (2019) 776-782. https://doi.org/10.1007/s10904-018-1051-0
- [23] D. E. Navarro-López, R. Garcia-Varela, O. Ceballos-Sanchez, A. Sanchez-Martinez, G. Sanchez-Ante, K. Corona-Romero, D. A. Buentello-Montoya, A. Elías-Zuñiga, E. R. López-Mena, Effective antimicrobial activity of ZnO and Yb-doped ZnO nanoparticles against Staphylococcus aureus and Escherichia coli, *Materials Science and Engineering: C* 123 (2021) 112004. https://doi.org/10.1016/j.msec.2021.112004
- [24] J._R. Camargo, I. A. A. Andreotti, C. Kalinke, J. M. Henrique, J. A. Bonacin, B. C. Janegitz, Waterproof paper as a new substrate to construct a disposable sensor for the electrochemical determination of paracetamol and melatonin, *Talanta* **208** (2020) 120458. https://doi.org/10.1016/j.talanta.2019.120458
- [25] B._P. Venkatachala, S. Manjappa, B. E. K. Swamy, L.S. Manjunatha, Pre-treated pencil graphite modified electrode sensor for melatonin, *Journal of Electrochemical Science and Engineering* **15** (2025) 2594. https://doi.org/10.5599/jese.2594
- [26] R. D. Crapnell, P. S. Adarakatti, C. E. Banks, Electroanalytical overview: the measurement of ciprofloxacin, Sensors and Diagnostics 3 (2024) 40-58. https://doi.org/10.1039/D3SD00129F
- [27] W._D. Adane, B. S. Chandravanshi, M. A. Tessema, A simple, ultrasensitive, and cost-effective electrochemical sensor for the determination of ciprofloxacin in various types of samples, *Sensing and Bio-Sensing Research* **39** (2023) 100547. https://doi.org/10.1016/j.sbsr.2022.100547
- [28] L. Mågeruşan, F. Pogåcean, B.-I. Cozar, S.-C. Tripon, S. Pruneanu, Harnessing Graphene-Modified Electrode Sensitivity for Enhanced Ciprofloxacin Detection, *International Journal of Molecular Sciences* **25** (2024) 3691. https://doi.org/10.3390/ijms25073691
- [29] T. Alizadeh, S. Amjadi, M. Akhoundian, Melatonin Determination at Trace Levels by ErO₂/MnO₂ Nanocomposite Modified Carbon Paste Electrode, *Analytical and. Bioanalytical Electrochemistry* **14** (2022) 1126-1137. https://www.abechem.com/article_700911_23a82eb97f8079eaa23b5bef56dc9568.pdf
- [30] G. I. Mohammed, A. L. Saber, Study of the Electrochemical Behavior of Melatonin on Different Electrodes in Aqueous Solution, *International Journal of Electrochemical Science* 15 (2020) 5895-5907. https://doi.org/10.20964/2020.06.90
- [31] R. C. Freitas, L. O. Orzari, L. M. C. Ferreira, T. R. L. C. Paixão, W. K. T. Coltro, F. C. Vicentini, B. C. Janegitz, Electrochemical determination of melatonin using disposable self-adhesive inked paper electrode, *Journal of Electroanalytical Chemistry* **897** (2021) 115550. https://doi.org/10.1016/j.jelechem.2021.115550
- [32] N. P. Shetti, S. J. Malode, D. Ilager, K. R. Reddy, S. S. Shukla, T. M. Aminabhavi, A Novel Electrochemical Sensor for Detection of Molinate Using ZnO Nanoparticles Loaded Carbon Electrode, *Electroanalysis* **31** (2019) 1040-1049. https://doi.org/10.1002/elan.201800775
- [33] N. P. Shetti, S. J. Malode, D. S. Nayak, G. B. Bagihalli, S. S. Kalanur, R. S. Malladi, Ch. V. Reddy, T. M. Aminabhavi, K. R. Reddy, Fabrication of ZnO nanoparticles modified sensor for electrochemical oxidation of methdilazine, *Applied Surface Science* **496** (2019) 143656. https://doi.org/10.1016/j.apsusc.2019.143656

- [34] L. S. Manjunatha, B. E. K. Swamy, Pre-Treated Cadmium Oxide Modified Carbon Paste Electrode Sensor for Catechol and Hydroquinone in the Presence of Resorcinol, *Analytical and Bioanalytical Electrochemistry* **15** (2023) 531-544. https://doi.org/10.22034/abec.2023.706505
- [35] L. S. Manjunatha, B. E. K. Swamy, S. C. Sharma, C. Sridhar, M. R. Sanjana, S. Kumar, Iron doped nickel oxide nanoparticle modified carbon paste electrode sensor for paracetamol in presence of ascorbic acid: A voltammetric study, *Materials Chemistry and Physics* **313** (2024) 128682. https://doi.org/10.1016/j.matchemphys.2023.128682
- [36] N. Kumar, N. E. Weerawarna, N. T. Alvarez, Carbon-Nanotube Microelectrodes for Electrochemical Determination of Melatonin, *Electroanalysis* **36** (2024) e202400191. https://doi.org/10.1002/elan.202400191
- [37] M. Isik, N. M. Gasanly, Gd-doped ZnO nanoparticles: Synthesis, structural and thermoluminescence properties, *Journal of Luminescence* **207** (2019) 220-225. https://doi.org/10.1016/j.jlumin.2018.11.022
- [38] K._A. Malik, J. H. Malik, A. A. Bhat, I. Assadullah, R. Tomar, Trap assisted visible light luminescent properties of hydrothermally grown Gd doped ZnO nanostructures, *Vacuum* **183** (2021) 109832. https://doi.org/10.1016/j.vacuum.2020.109832
- [39] M._I. Ghouri, E. Ahmed, N. R. Khalid, M. Ahmad, M. Ramzan, A. Shakoor, N. A. Niaz, Gadolinium doped ZnO nanocrystalline powders and its photocatalytic performance for degradation of methyl blue under sunlight, *Journal of Ovonic Research* **10** (2014) 89-100.
- [40] P. G. Ramos, J. Espinoza, L. A. Sánchez, J. Rodriguez, Enhanced photocatalytic degradation of Rhodamine B employing transition metal (Fe, Cu, Co) doped ZnO/rGO nanostructures synthesized by electrospinning-hydrothermal technique, *Journal of Alloys and Compounds* **966** (2023) 171559. https://doi.org/10.1016/j.jallcom.2023.171559
- [41] M. Sellam, S. Azizi, D. Bouras, M. Fellah, A. Obrosov, G. A. El-Hiti, Degradation of rhodamine B dye under visible and solar light on zinc oxide and nickel-doped zinc oxide thin films, *Optical Materials* **151** (2024) 115316. https://doi.org/10.1016/j.optmat.2024.115316
- [42] M. Ahmad, W. Rehman, M. M. Khan, M. T. Qureshi, A. Gul, S. Haq, R. Ullah, A. Rab, F. Menaa, Phytogenic fabrication of ZnO and gold decorated ZnO nanoparticles for photocatalytic degradation of Rhodamine B, *Journal of Environmental Chemical Engineering* **9** (2021) 104725. https://doi.org/10.1016/j.jece.2020.104725
- [43] Q. Yin, R. Qiao, Z. Li, X. L. Zhang, L. Zhu, Hierarchical nanostructures of nickel-doped zinc oxide: Morphology controlled synthesis and enhanced visible-light photocatalytic activity, *Journal of Alloys and Compounds* **618** (2015) 318-325. https://doi.org/10.1016/j.jallcom.2014.08.087

©2025 by the authors; licensee IAPC, Zagreb, Croatia. This article is an open-access article distributed under the terms and conditions of the Creative Commons Attribution license (https://creativecommons.org/licenses/by/4.0/)

